Flexible Electrospun Carbon Nanofiber@NiS Core/Sheath Hybrid Membranes as Binder-Free Anodes for Highly Reversible Lithium Storage

Longsheng Zhang, Yunpeng Huang, Youfang Zhang, Huahao Gu, Wei Fan, and Tianxi Liu**

The lithium storage performance of metal sulfides is restricted by their intrinsic poor conductivity, large volumetric expansion, and involvement of insulating polymer binders during the electrode preparation process, which can be solved by constructing binder-free hybrid electrodes with nanostructured metal sulfides grown on self-standing conductive templates. In this work, flexible hybrid membranes with nickel sulfide (NiS) nanoparticles uniformly anchored on electrospun carbon nanofibers (CNFs) have been prepared as binder-free anodes for high-performance lithium-ion batteries. The hierarchical CNF@NiS core/sheath hybrid membranes with 3D macroporous architecture can provide open and continuous channels for rapid diffusion of lithium ions to access the electrochemically active NiS nanoparticles. Moreover, the CNF can act as both a conductive core to provide efficient transport of electrons for fast lithiation/delithiation of the NiS sheath, and as a buffering matrix to mitigate the local volumetric expansion/contraction upon long-term cycling. As a consequence, the optimized CNF@NiS hybrid membranes exhibit a high reversible capacity of 1149.4 mA h g^{-1} with excellent cycling stability, and high rate capability of 664.3 mA h g^{-1} even at a high current density of 3 A g^{-1}, making them promising flexible and binder-free anode materials for highly reversible lithium storage.

1. Introduction

With ever-increasing demand for efficient energy storage, extensive efforts have been devoted to develop advanced energy storage and conversion systems, such as lithium-ion batteries (LIBs), supercapacitors, solar cells, fuel cells, etc.[1–6] Among them, LIBs have become one of the predominant power sources for applications in portable electronic devices, electric vehicles, and hybrid electric vehicles, owing to their high energy density, long cycle life, and environmental benignity.[7] Currently, commercialized graphite is the most widely used anode material for LIBs, but it cannot meet the requirements for high-performance LIBs due to its relatively low theoretical specific capacity (372 mA h g^{-1}).[8] Therefore, the ongoing search for alternative anode materials with high specific capacity and good cycling stability has become the subject of intensive research worldwide.[9–13]

Recently, metal sulfides (e.g., FeS, NiS, MoS_2, SnS_2, etc.) have attracted tremendous attention as promising anode materials for next-generation LIBs due to their higher theoretical capacities.[14–20] In particular, nickel sulfide (NiS) has a high theoretical capacity (590 mA h g^{-1}) as well as many excellent properties including good electronic conductivity, abundant resources, and low toxicity.[21–24] However, the practical applications of NiS materials are severely hindered by their rapid capacity fade upon cycling, which mainly results from their large volumetric expansion and serious agglomeration during the repetitive lithiation/delithiation process.[25–27] In order to achieve high reversible capacities and long cycling life, one effective strategy is to optimize the NiS materials to nanostructures and confine them within a conductive carbonaceous matrix, which can act both as a buffer to accommodate the volume expansion/contraction, and as a separator to inhibit NiS particles from aggregating during the long-term cycling.[28–33] Moreover, it can also offer a conductive scaffold to maintain reliable electric contact with NiS materials and facilitate the charge transport across the interfaces, resulting in greatly enhanced reversible capacity and cycling stability.[34–36] For instance, nanocomposites of ultrathin NiS nanosheets and graphene sheets delivered substantially higher specific capacities and better cyclic stability compared with pure NiS nanosheets.[37] Similarly, a synergistic effect was also achieved from hybrid materials with NiS nanorod-assembled nanoflowers grown on

L. S. Zhang, Y. P. Huang, Y. F. Zhang,
H. H. Gu, Prof. T. X. Liu
State Key Laboratory of
Molecular Engineering of Polymers
Department of Macromolecular Science
Fudan University
Shanghai 200433, P. R. China
E-mail: txliu@fudan.edu.cn

Dr. W. Fan, Prof. T. X. Liu
State Key Laboratory of Modification
of Chemical Fibers and Polymer Materials
College of Materials Science and Engineering
Donghua University
Shanghai 201620, P. R. China
E-mail: 10110440003@fudan.edu.cn

DOI: 10.1002/admi.201500467

graphene, where enhanced electrical contact, electrode structure stability, and reduced Li-ion diffusion pathways were obtained, leading to greatly improved lithium storage capacity and cycling performance.[38] However, these NiS-based electrode materials need to be mixed with conductive additives and polymer binders for the battery tests, which is complicated and time-consuming.[39] Besides, the polymer binders are insulating and electrochemically inert, which may severely block the diffusion channels of ion transportation and impair the overall electrochemical performance of electrode materials.[40] Thus, a proper self-standing substrate with high electrical conductivity and mechanical flexibility for fabricating binder-free NiS-based electrode is highly desirable for the improvement of its lithium storage performance.

Here, we demonstrate an efficient and scalable process to fabricate flexible hybrid membranes of electrospun CNF@NiS core/sheath fibers as binder-free anodes for LIBs. First, flexible self-standing CNF membranes with unique 3D fiber networks and excellent structural stability are facilely obtained through the combination of electrospinning and carbonization (as shown in **Figure 1**). Then, hierarchical nanostructures are conveniently constructed with nanosized NiS particles uniformly anchored on the CNFs, which can effectively prevent the agglomeration of NiS nanoparticles and mitigate their volumetric expansion during the repetitive cycling process. Additionally, the conductive CNF core can provide efficient transport of electrons for fast lithiation/delithiation of the electrochemically active NiS sheath. Moreover, the 3D macroporous architecture derived from the nanofiber networks can significantly increase the porosity and facilitate the rapid diffusion of lithium ions to access the NiS nanoparticles. As a result of the synergistic effects between CNF and NiS, the optimized electrospun CNF@NiS core/sheath hybrid membranes exhibit a high reversible capacity of 1149.4 mA h g^{-1} as well as excellent cycling stability and rate capability, showing great potential as flexible anode materials for high-performance LIBs.

2. Results and Discussion

2.1. Morphology and Structure of CNF@NiS Core/Sheath Hybrid Membranes

Electrospinning is a simple and efficient technique for fabricating self-standing nanofiber membranes with unique 3D fiber networks, good structural stability, and high flexibility.[41–45] As shown in **Figure 2**, the electrospun CNFs have an average diameter of about 200–300 nm and smooth surfaces without defects. Moreover, the nanofibers interconnected with each other are able to form a 3D open architecture, which can provide a high-surface-area template for further growth of electrochemically active materials to construct hierarchical nanocomposites. In this work, a facile low-temperature chemical bath deposition (CBD) process was utilized to in-situ grow crystalline $Ni(OH)_2$ nanosheets on CNFs (**Figure 3**). It can be seen that the loading amount of $Ni(OH)_2$ nanosheets on nanofibers obviously increases with increasing concentrations of $Ni(NO_3)_2$ solution used in the preparation procedure. As for the CNF@$Ni(OH)_2$-1 hybrid membrane (Figure 3A,D), only small $Ni(OH)_2$ flakes are evenly scattered on nanofibers under a low dosage of $Ni(NO_3)_2$. With increasing $Ni(NO_3)_2$ concentration, thin $Ni(OH)_2$ nanosheets with curled shapes begin to form and grow perpendicularly on the surface of nanofibers (Figure 3B,E). However, a thick layer of $Ni(OH)_2$ nanosheets and large $Ni(OH)_2$ agglomerates are gradually formed with further increasing concentrations of $Ni(NO_3)_2$ (Figure 3C,F), which may be attributed to the rapid homogeneous nucleation of $Ni(OH)_2$ under high concentrations. As exhibited in Figure S1 (Supporting Information), pure $Ni(OH)_2$ nanosheets produced in the absence of CNF membranes severely aggregate into much larger spherical agglomerates. Thus, constructing hierarchical nanostructures with $Ni(OH)_2$ nanosheets uniformly grown on the CNFs can effectively prevent the aggregation of $Ni(OH)_2$ nanosheets.

After sulfidation treatment of the CNF@$Ni(OH)_2$ hybrid membranes in ethanol solution of thioacetamide,

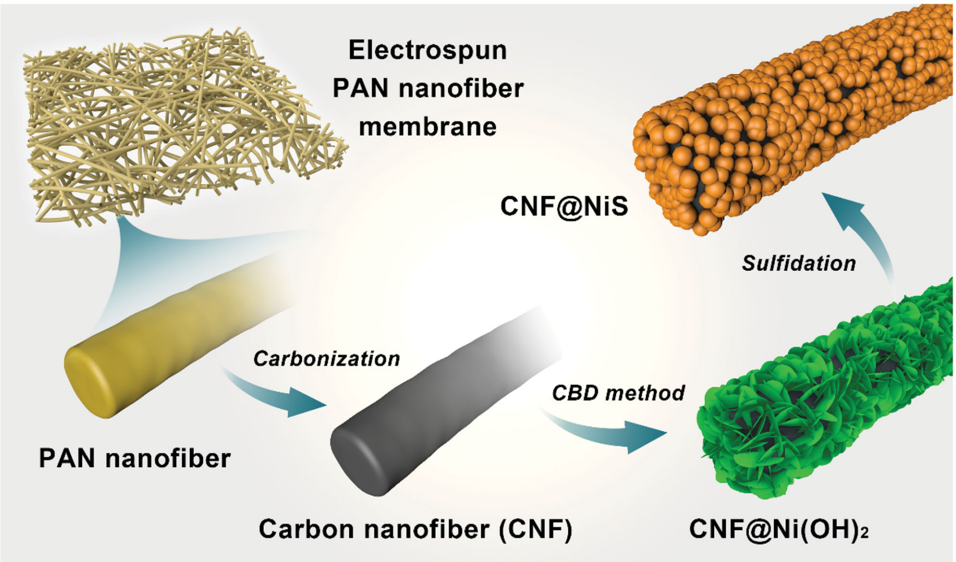

Figure 1. Schematic illustration of the preparation of flexible free-standing CNF@NiS core/sheath hybrid membranes.

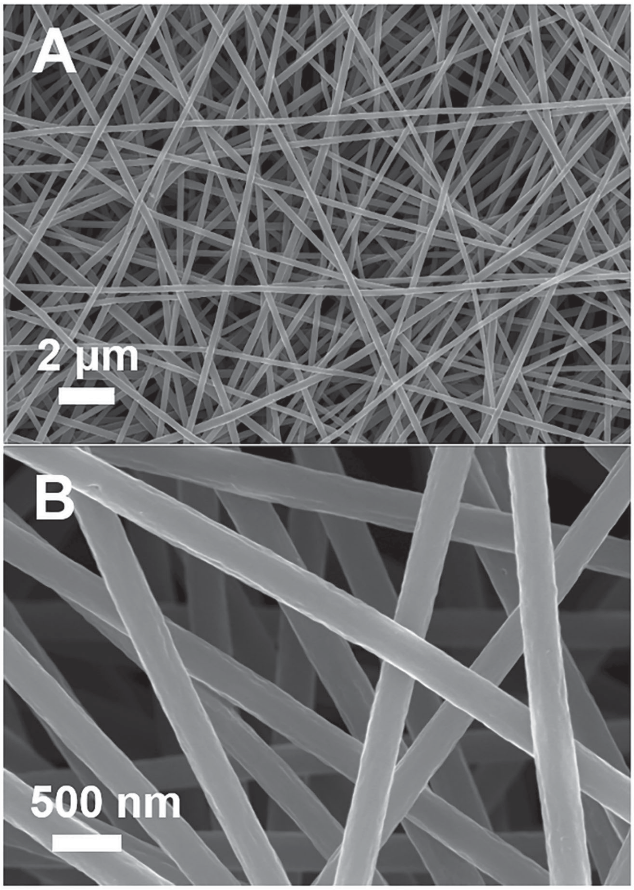

Figure 2. Field emission scanning electron microscope (FESEM) images of a CNF membrane at A) low and B) high magnifications.

CNF@NiS hybrid membranes with NiS nanoparticles anchored on the CNFs are obtained (**Figure 4**). Owing to the S^{2-} ion exchange reactions, nanosheet-like $Ni(OH)_2$ are transformed into nanoparticle-like NiS via three reactions as described by the following Equations (1)–(3)[46]

$$CH_3CSNH_2 + C_2H_5OH \rightarrow CH_3(NH_2)C(OC_2H_5) - SH \tag{1}$$

$$\begin{aligned} &CH_3(NH_2)C(OC_2H_5) - SH + C_2H_5OH \\ &\quad \rightarrow CH_3(NH_2)C(OC_2H_5)_2 + H_2S \end{aligned} \tag{2}$$

$$H_2S + Ni(OH)_2 \rightarrow NiS + 2H_2O \tag{3}$$

The content of NiS nanoparticles in the CNF@NiS hybrid membranes clearly increases with increasing initial loading amounts of $Ni(OH)_2$ nanosheets on CNFs. As shown in Figure 4A,D, the nanofibers of CNF@NiS-1 hybrid membranes have not been fully covered by NiS nanoparticles due to the low loading amount of $Ni(OH)_2$ nanosheets. For the CNF@NiS-2 hybrid membrane, NiS nanoparticles with diameters of 30–70 nm are uniformly distributed on the nanofibers (Figure 4B,E), thus preventing the aggregation of NiS nanoparticles and providing a 3D macroporous structure that is beneficial for rapid diffusion of lithium ions to access active materials during the lithiation/delithiation processes. From Figure 4C,F, the NiS nanoparticles are densely accumulated and form a thick layer on the nanofibers of CNF@NiS-3 hybrid membranes, which will surely deteriorate the electron transport between NiS nanoparticles and the conductive CNFs. In comparison, the pure NiS nanoparticles sulfurated from pure $Ni(OH)_2$ nanosheets tend to aggregate with each other and form large agglomerates (Figure S2, Supporting Information), implying the significance of CNFs for effectively dispersing NiS nanoparticles. Brunauer–Emmett–Teller (BET) analysis (Figure S3, Supporting Information) strongly verifies the CNF@NiS-2 hybrid membranes as mesoporous materials with much larger specific surface area than the nonporous NiS powder. The specific surface area and pore volume for a CNF@NiS-2 hybrid membrane are 89.2 m^2 g^{-1} and 0.38 cm^3 g^{-1}, respectively, which are much larger than those of pure NiS powder (7.5 m^2 g^{-1} and 0.06 cm^3 g^{-1}). As shown in the inset of Figure S3 (Supporting Information), the pore size distribution of CNF@NiS-2 hybrid membrane calculated from the Barrett–Joiner–Halenda method is mainly centered at 4 nm, which is in the mesoporous range. The larger specific surface area and pore volume of CNF@NiS-2 hybrid membrane can greatly facilitate rapid diffusion of electrolyte to access the electrochemically active NiS nanoparticles, thus leading to significantly improved lithium storage performance compared with pure NiS powder. Furthermore, it is worthy to mention that no crack was observed upon bending of the CNF@NiS-2 hybrid membrane (inset of Figure 4E), indicating its high flexibility as binder-free anode for LIBs, which can avoid the cumbersome slurry coating process for preparing NiS-based composite electrodes by using conductive additives and polymer binders as reported previously.[47–49]

The complete conversion from CNF@$Ni(OH)_2$ to CNF@NiS is corroborated by X-ray diffraction (XRD) analysis (**Figure 5**). Both the pure $Ni(OH)_2$ and CNF@$Ni(OH)_2$-2 hybrid membranes display four diffraction peaks at $2\theta = 12.3°$, 24.6°, 33.8°, and 59.8°, corresponding to (003), (006), (101), and (110) planes of α-$Ni(OH)_2$ (JCPDS 38–0715), respectively. Moreover, a broad peak ranging from 20° to 30° is observed in the XRD pattern of CNF@$Ni(OH)_2$-2 hybrid membrane, which is ascribed to amorphous CNFs, indicating the coexistence of $Ni(OH)_2$ and CNFs in CNF@$Ni(OH)_2$ hybrid membranes. As for pure NiS and CNF@NiS-2 hybrid membranes, five new peaks located at $2\theta = 30.4°$, 34.9°, 46.0°, 53.7°, and 73.1° can be indexed to (100), (101), (102), (110), and (202) planes of α-NiS (JCPDS 02–1280) respectively. And all the peaks related to $Ni(OH)_2$ completely disappear, which unambiguously verifies the successful conversion of CNF@$Ni(OH)_2$ to CNF@NiS after the sulfidation treatment.[50] Additionally, the Raman spectra of a CNF membrane and a CNF@NiS-2 hybrid membrane (Figure S4, Supporting Information) both exhibit two strong peaks located at 1345 and 1588 cm^{-1}, while the Raman spectrum of pure NiS powder shows no peak in the range from 1100 to 1900 cm^{-1}. These two peaks are consistent with the well-known D (disorder) and G (graphite) band peaks, which are ascribed to the sp^3 and sp^2 hybridized carbons, representing the disordered and well-ordered lattice structures, respectively.[51] Moreover, the intensity of the G-band peak is relatively higher, which indicates its high degree of crystallinity in the lattice structure of the CNFs.[52] Moreover, the weight ratios of CNF in CNF@NiS hybrid membranes can be calculated from thermogravimetric analysis (TGA) analysis (Figure S5, Supporting Information),

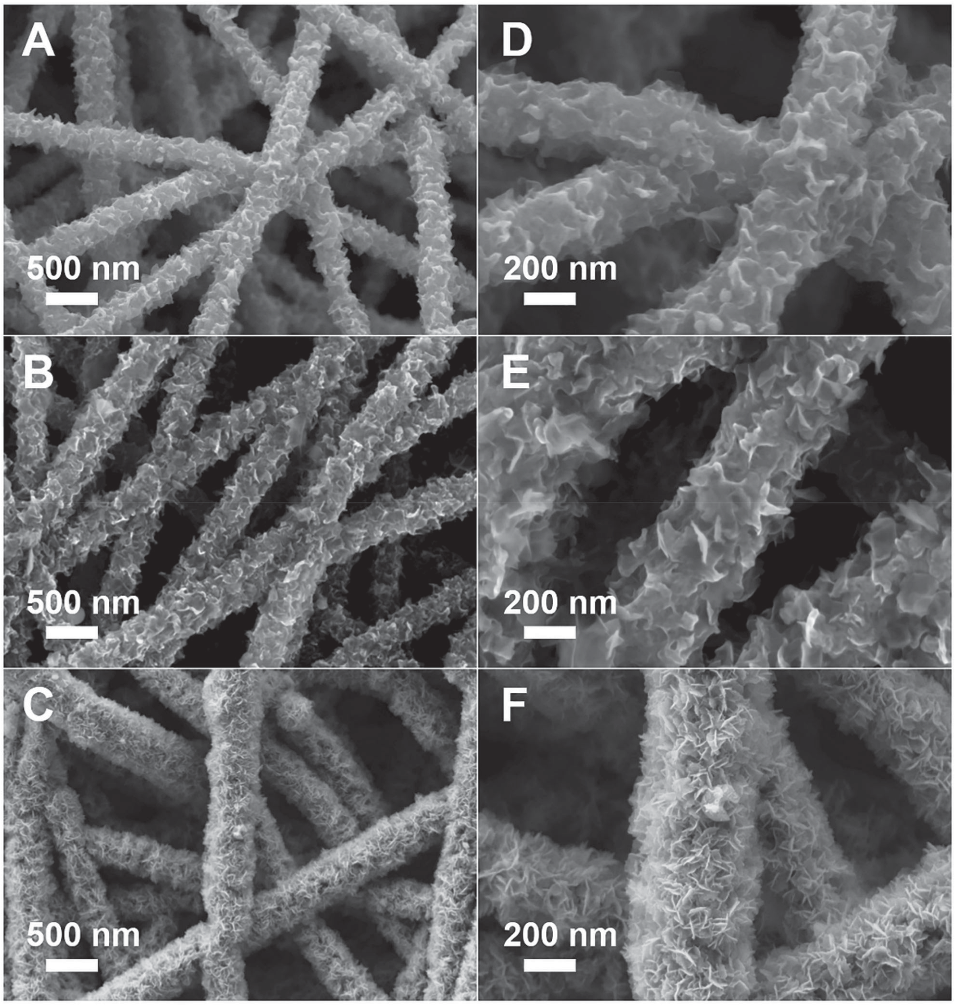

Figure 3. Low (left) and high (right) magnification FESEM images of A,D) CNF@Ni(OH)$_2$-1, B,E) CNF@Ni(OH)$_2$-2, and C,F) CNF@Ni(OH)$_2$-3 hybrid membranes.

which are 68.5, 48.0, and 37.7 wt% for CNF@NiS-1, CNF@NiS-2, and CNF@NiS-3 hybrid membranes, respectively.

The surface electronic state and composition of CNF@NiS-2 hybrid membranes were further investigated by X-ray photoelectron spectroscopy (XPS) analysis as presented in **Figure 6**. Characteristic peaks for Ni, S, C, and O elements with no detectable impurities are observed in the survey spectrum (Figure 6A), which are consistent with energy dispersive spectroscopy results (Figure S6, Supporting Information). A high-resolution spectrum of Ni 2p shows a strong main peak at 853.2 eV assigned to Ni 2p$_{3/2}$, as well as an associated excited final state satellite peak located at 7.8 eV, a higher binding energy than the main peak (Figure 6B), in good agreement with those reported previously for NiS.[53] The peak centered at 856.0 eV and its associated higher binding energy satellite at 7.7 eV can be attributed to nickel–oxygen species on the sample surface due to the exposure to atmospheric oxygen.[54] Similarly, two characteristic peaks corresponding to the binding energies of Ni 2p$_{1/2}$ and its associated oxygenated component appear at 870.6 and 874.1 eV, respectively. In the high resolution S 2p spectrum (Figure 6C), the peaks located at 162.9 and 161.7 eV are assigned to S 2p$_{1/2}$ and S 2p$_{3/2}$ orbitals of divalent sulfide ions (S^{2-}), respectively. Moreover, the detailed compositional analysis reveals that the surface Ni:S atomic ratio is 1.06:1, which is close to the formula of NiS. Figure 6D presents the high resolution C 1s spectrum of a CNF@NiS-2 hybrid membrane, showing a standard carbon peak at 284.6 eV.

2.2. Electrochemical Performance of CNF@NiS Core/Sheath Hybrid Membranes

In order to evaluate the electrochemical performance, flexible free-standing CNF@NiS hybrid membranes were directly used as binder-free anodes and assembled into coin cells. To investigate the electrochemistry during the cell testing process, cyclic voltammetry (CV) curves of the 1st, 2nd, and 5th cycles of a CNF@NiS-2 hybrid membrane were collected in the potential window of 0.01–3.0 V at a scan rate of 0.1 mV s^{-1} (**Figure 7**A). In the initial cathodic scan, two reduction peaks at about 1.1 and 0.6 V are observed, corresponding to the formation of Ni and solid electrolyte interface (SEI) films, respectively.[39] During the

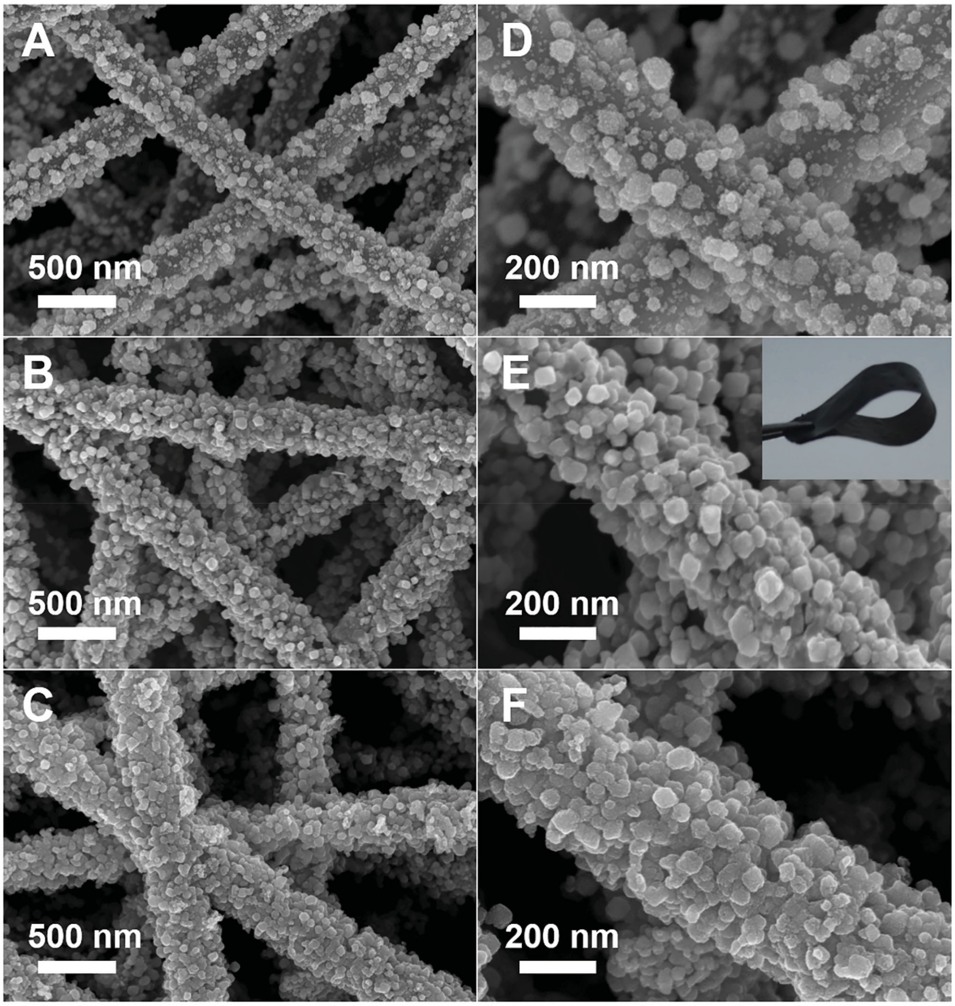

Figure 4. Low (left) and high (right) magnification FESEM images of A,D) CNF@NiS-1, B,E) CNF@NiS-2, and C,F) CNF@NiS-3 hybrid membranes. The inset of (E) shows the corresponding digital photo of the highly flexible CNF@NiS-2 hybrid membrane.

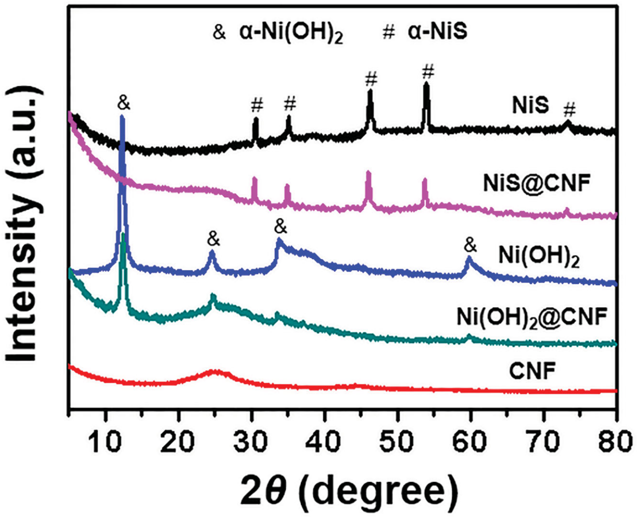

Figure 5. XRD patterns of CNF membrane, pure $Ni(OH)_2$, pure NiS, CNF@$Ni(OH)_2$, and CNF@NiS hybrid membranes.

subsequent cycles, two cathodic peaks located at about 1.7 and 1.3 V are attributed to the two-step electrochemical reactions between NiS and lithium. According to Equations (4) and (5), NiS reacts with lithium to form intermediate products of Ni_3S_2 and Li_2S at the first stage and then form Ni and Li_2S at the second stage.[38] The transformation from NiS to Ni_3S_2 is related to the cathodic peak at 1.7 V, while the cathodic peak at 1.3 V is associated with that from Ni_3S_2 to Ni. In the anodic scan for the initial and subsequent cycles, four peaks at 1.1, 1.5, 2.1, and 2.3 V are observed, which can be ascribed to the formation of NiS and decomposition of SEI layer.[55] To be noticed, the CV curves of the subsequent cycles are almost overlapped, indicating an excellent reversibility of the CNF@NiS-2 hybrid membrane during the lithiation/delithiation process.

$$3NiS + 2Li \leftrightarrow Ni_3S_2 + Li_2S \tag{4}$$

$$Ni_3S_2 + 4Li \leftrightarrow 3Ni + 2Li_2S \tag{5}$$

Figure 7B presents the galvanostatic discharge–charge profiles (1st, 2nd, and 5th cycles) of the CNF@NiS-2 hybrid membrane at a current density of 0.1 A g^{-1}. There are two

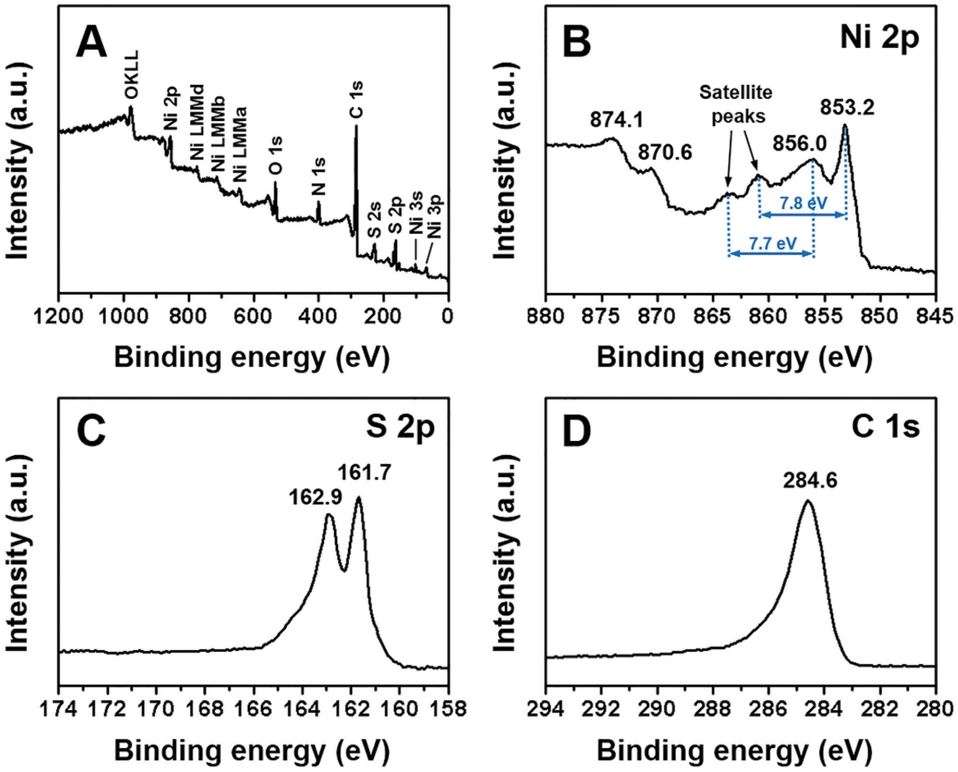

Figure 6. A) XPS survey spectrum, high resolution B) Ni 2p spectrum, C) S 2p spectrum, and D) C 1s spectrum of a CNF@NiS-2 hybrid membrane.

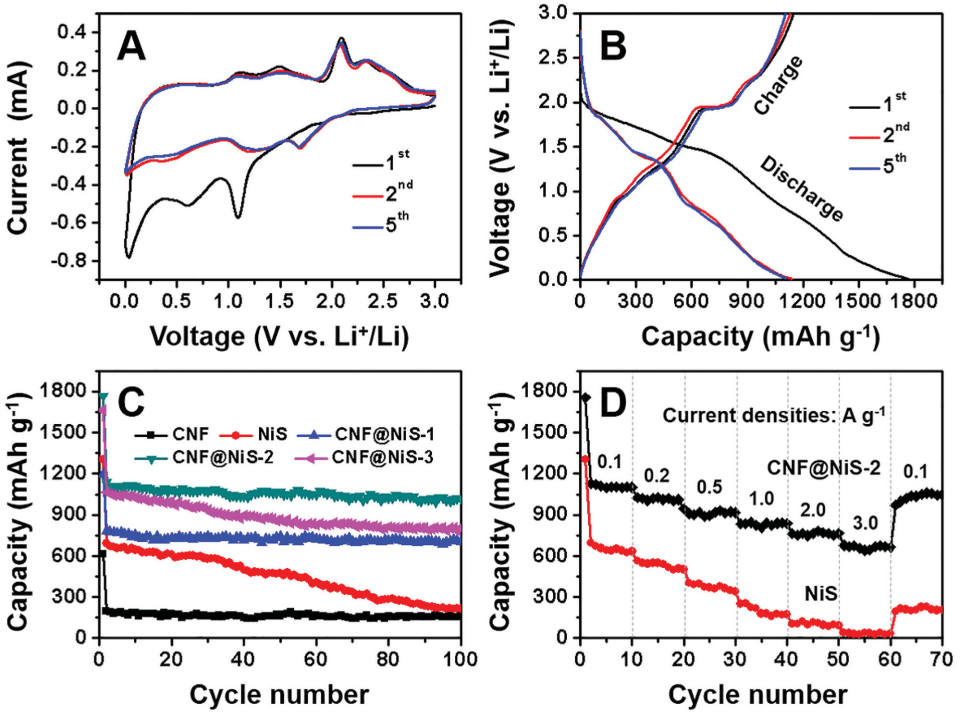

Figure 7. A) CV curves (1st, 2nd, and 5th cycles) of the CNF@NiS-2 hybrid membrane measured at a scan rate of 0.1 mV s^{-1}. B) The discharge/charge curves of the CNF@NiS-2 hybrid membrane in the 1st, 2nd, and 5th cycles. C) Cycling performance of the CNF membrane, pure NiS powder, CNF@NiS-1, CNF@NiS-2, and CNF@NiS-3 hybrid membranes at a current density of 0.1 A g^{-1}. D) Rate performance of pure NiS powder and the CNF@NiS-2 hybrid membrane at various current densities.

potential plateaus at 1.2 and 0.6 V in the first discharge curve, corresponding to the formation of a Ni and SEI layer, which is in accordance with the CV results. For the subsequent discharge cycles, two plateaus located at 1.7 and 1.3 V are also consistent with the CV analysis, indicating the two-step lithiation process of NiS (Equations (4) and (5)). During the charge process, the potential plateau located at 1.0, 1.4, 2.0, and 2.3 V can be attributed to the reversible formation of NiS and decomposition of SEI layer. As for the pure CNF membrane, only one flat potential plateau at about 0.25 V in the first discharge curve is observed and the plateaus mentioned above for the CNF@NiS-2 hybrid membrane are not observed (Figure S7, Supporting Information). In the initial cycle, the discharge and charge capacities of pure NiS are 1305.5 and 715.3 mA h g^{-1}, respectively, with an initial Columbic efficiency of 55%. In contrast, the initial discharge and charge capacities of the CNF@NiS-2 hybrid membrane are 1768.9 and 1149.4 mA h g^{-1}, respectively, with initial Columbic efficiency of 65%. The greatly improved reversible capacities can be ascribed to the uniform distribution of NiS nanoparticles on conductive CNFs instead of forming aggregations as well as the enhanced kinetics of charge transfer across the interfaces. Additionally, the 3D hierarchical nanostructures of CNF@NiS-2 hybrid membranes can greatly increase the porosity and facilitate the rapid diffusion of lithium ions to access the NiS nanoparticles. On the contrary, as for pure NiS, the aggregation of NiS nanoparticles makes it difficult to realize full lithiation of their internal portion and the involvement of insulating polymer binders during the NiS electrode preparation may severely deteriorate the overall lithium storage performance.

Not only high reversible capacity but also good cyclic stability is desirable for promising anode materials in LIBs. Figure 7C demonstrates the cycling performance of pure NiS, CNF, CNF@NiS-1, CNF@NiS-2, and CNF@NiS-3 hybrid membranes at a current density of 0.1 A g^{-1}. The pure CNF membrane manifests excellent cyclic stability, but its reversible capacity is only about 160 mA h g^{-1}. Although the NiS electrode has an initial charge capacity of 715.3 mA h g^{-1}, it shows severe capacity decay and only delivers a reversible capacity of 215.6 mA h g^{-1} after 100 cycles. The rapid capacity fade of pure NiS is due to their intrinsic poor conductivity, serious aggregation, and pulverization during the cycling process. By comparison, the CNF@NiS-1, CNF@NiS-2, and CNF@NiS-3 hybrid membranes deliver much higher reversible capacities of 706.3, 1020.6, and 805.8 mA h g^{-1} after 100 cycles, respectively. Additionally, the Columbic efficiency of CNF@NiS-2 hybrid membrane gradually achieves nearly 100% after several cycles (Figure S8, Supporting Information), further indicating its excellent cyclic stability upon long-term cycling. The remarkably improved cycling performance of CNF@NiS hybrid membranes can be attributed to the CNF matrix that restrains the agglomeration of NiS nanoparticles and avoids the loss of sulfide intermediates during repetitive lithium storage/release process. As displayed in Figure S9 (Supporting Information), the field emission scanning electron microscope (FESEM) image of CNF@NiS-2 hybrid membrane after the cycling test shows that the NiS nanoparticles are still uniformly covered on the surface of CNFs, confirming that the CNF core plays an important role in accommodating the volumetric expansion/contraction of NiS nanoparticles and maintaining the structural stability of the CNF@NiS-2 hybrid membrane upon long-term cycling. Among these materials, CNF@NiS-2 hybrid membrane exhibits the highest reversible capacity, which can be ascribed to the optimized amount of NiS nanoparticles anchored on the CNFs as well as the better electrical contact and interfacial interaction between the NiS sheath and conductive CNF core. Associated with the morphology analysis, the nanofibers of CNF@NiS-1 hybrid membrane have not been fully covered by NiS nanoparticles, while the densely accumulated NiS nanoparticles already form agglomerates on the nanofibers of the CNF@NiS-3 hybrid membrane (Figure 4). Thus, it gives a proper explanation for the optimized electrochemical performance of the CNF@NiS-2 hybrid membrane, in which the CNFs are fully and uniformly covered by NiS nanoparticles with less aggregation.

The rate capabilities of pure NiS powder and the CNF@NiS-2 hybrid membrane were investigated by applying various current densities on the coin cells (Figure 7D). The reversible capacity of pure NiS fades to less than 50 mA h g^{-1} as the current density increases to 3 A g^{-1}, and regains a capacity of about 205.6 mA h g^{-1} (only about 29% of the initial charge capacity) when the current density decreases back to 0.1 A g^{-1}. Contrarily, the CNF@NiS-2 hybrid membrane delivers a high reversible capacity of 664.3 mA h g^{-1} as the current density increases to 3 A g^{-1}. Moreover, the reversible capacity restores to 1048.5 mAh g^{-1} when the current rate is changed back to 0.1 A g^{-1}, approaching 91% of its initial charge capacity. Rate performances of different CNF@NiS hybrid membranes (Figure S10, Supporting Information) further reveal that the CNF@NiS-2 hybrid membrane exhibits higher reversible capacities over those of CNF@NiS-1 and CNF@NiS-3 hybrid membranes under various current densities. Furthermore, the capacities of the CNF@NiS-2 hybrid membrane can still be retained at 745.2, 640.7, and 543.8 mA h g^{-1} at 1, 2, and 3 A g^{-1} after 100 cycles respectively, indicating its excellent cycling stability at high current densities (**Figure 8**). The remarkably enhanced cyclic stability and rate capability of CNF@NiS hybrid membranes are ascribed to the synergistic effects between CNFs and NiS nanoparticles, where the highly

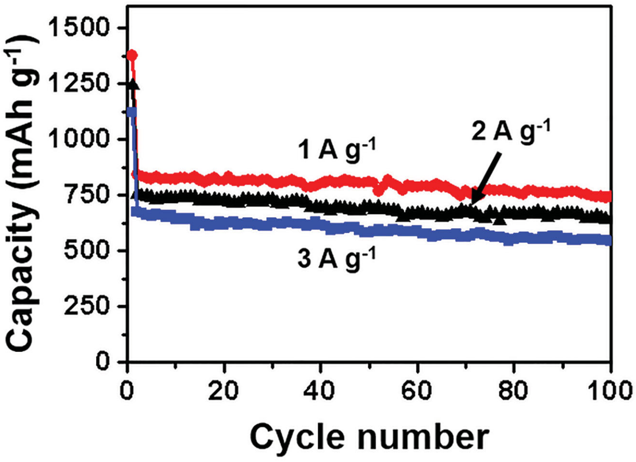

Figure 8. High-rate cycling performance of the CNF@NiS-2 hybrid membrane in the voltage range from 0.01 to 3.0 V at current densities of 1, 2, and 3 A g^{-1}.

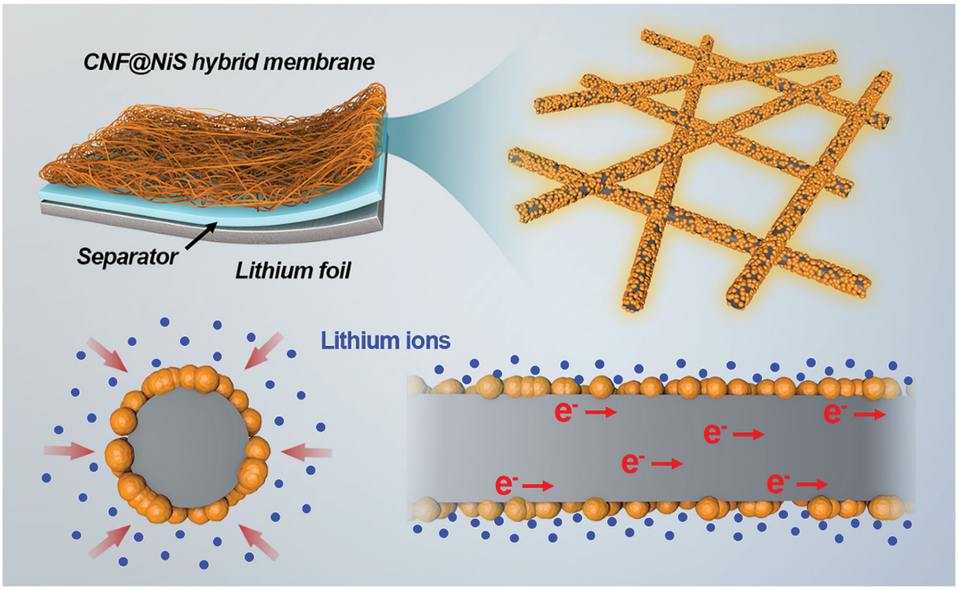

Figure 9. Schematic illustration of lithium ion diffusion and electron transportation in CNF@NiS core/sheath hybrid membranes.

conductive CNFs can act as the conductive core to provide efficient electron transport for fast lithiation/delithiation of the electrochemically active NiS sheath (**Figure 9**). Moreover, the overall 3D macroporous architectures as well as the hierarchical nanostructures of CNF@NiS-2 hybrid membrane can significantly shorten the lithium ion diffusion length, enhance the contact area and ensure the ion and electron diffusion with little resistance, leading to greatly improved lithium storage performance.

To better understand the superior electrochemical performance of CNF@NiS core/sheath hybrid membranes, electrochemical impedance spectroscopy (EIS) measurements were carried out to investigate the electrochemical impedance of the CNF membrane, pure NiS powder, and the CNF@NiS-2 hybrid membrane as shown in **Figure 10**. The Nyquist plots consist of two semicircles at high and medium frequencies and a straight line with a constant inclining angle at low frequencies, which are related to the resistance of the SEI, charge-transfer resistance at the electrolyte/electrode interface and the solid-state diffusion resistance of lithium ions in the electrode, respectively. It can be clearly seen that the CNF@NiS-2 electrode displays a much smaller radius of semicircle in the high-medium frequency region compared to that of pure NiS electrode. The electrode–electrolyte interfacial resistances (R_i) are 65, 104, and 133 Ω for CNF membrane, CNF@NiS-2 hybrid membrane and pure NiS powder, respectively. The remarkably reduced R_i value of CNF@NiS-2 hybrid membrane compared with that of pure NiS powder indicates the greatly reduced charge-transfer resistance at the electrode/electrolyte interface due to the combination of NiS sheath with the conductive nanofiber core, which can greatly facilitate the rapid transfer of both lithium ions and electrons during the lithiation/delithiation process and result in highly reversible lithium storage.

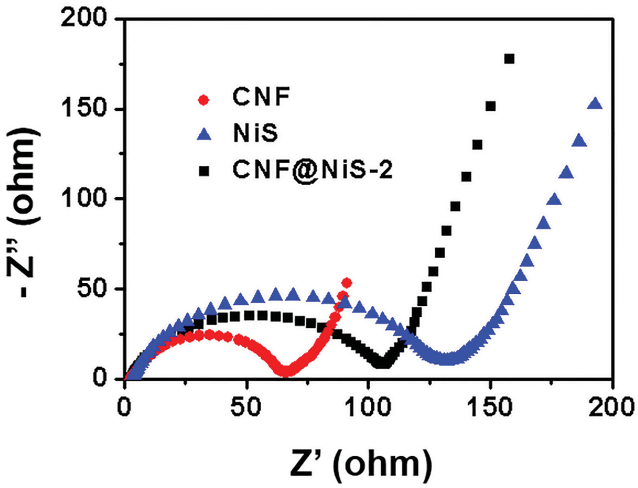

Figure 10. Nyquist plots of CNF membrane, pure NiS powder, and CNF@NiS-2 hybrid membrane measured in the frequency range from 100 kHz to 0.01 Hz with an AC voltage amplitude of 5.0 mV.

3. Conclusions

In summary, highly flexible CNF@NiS core/sheath hybrid membranes with NiS nanoparticles uniformly anchored on the electrospun CNFs have been facilely prepared as binder-free anodes for high-performance LIBs. The CNFs with excellent electrical conductivity and structural stability cannot only facilitate the charge transfer across the interfaces for fast lithiation/delithiation of the NiS sheath, but also effectively mitigate the aggregation and volumetric expansion/contraction of NiS nanoparticles upon long-term cycling. Moreover, the overall 3D macroporous architectures as well as the hierarchical nanostructures of CNF@NiS hybrid membranes can significantly increase the porosity and enable rapid diffusion of lithium ions to access electrochemically active NiS nanoparticles. Benefiting from the synergistic effects, remarkably improved lithium storage performance has been achieved for the optimized CNF@NiS hybrid membrane with a high reversible capacity of 1149.4 mA h g^{-1} and excellent cyclic stability, as well as a high-rate capability of 664.3 mA h g^{-1} even at a high current density of 3 A g^{-1}, making it a promising candidate as a flexible and binder-free anode material for highly reversible lithium storage.

4. Experimental Section

Materials: Polyacrylonitrile (PAN) (M_w = 150 000 g mol^{-1}) was purchased from Sigma-Aldrich. Electrolyte (1 M $LiPF_6$ in ethylene carbonate (EC)/dimethyl carbonate (DMC)/diethyl carbonate (DEC) (1:1:1 by volume)), lithium foil, and Celgard-2400 were purchased from Shanxi Lizhiyuan Co. Ltd. All other reagents were purchased from Sinopharm Chemical Reagent Co. Ltd. and used as received without further purification. Deionized water was used throughout all the experiments.

Preparation of CNF@NiS Core/Sheath Hybrid Membranes: The preparation procedure of electrospun CNF@NiS core/sheath hybrid membranes was schematically illustrated in Figure 1. PAN nanofiber membrane was first synthesized through a simple single-nozzle electrospinning technique. Typically, 1 g PAN was dissolved in 5 mL *N,N*-dimethylformamide (DMF) at room temperature under vigorous stirring to form viscous transparent solution and then transferred into a 5 mL plastic syringe. The electrospinning process was carried out at an applied voltage of 20 kV with a feeding rate of 0.25 mm min^{-1} through a stainless steel needle positioned 20 cm away from the aluminum drum collector. The generated PAN nanofiber membrane was preoxidized at 250 °C in an air atmosphere for 1 h with a heating rate of 1 °C min^{-1}, and then carbonized in a conventional tube furnace at 800 °C for 2 h in N_2 atmosphere to obtain CNF. After that, CNF@Ni$(OH)_2$ core/sheath hybrid membranes with different loading amounts of $Ni(OH)_2$ were prepared by a CBD method. Briefly, certain amounts of $Ni(NO_3)_2·6H_2O$ (i.e., 145, 290, and 580 mg, respectively) and 500 mg urea were dissolved into a mixed solution of 20 mL deionized water and 20 mL ethyl alcohol under stirring. The CNF membranes were then immersed in the above solution and heated to 70 °C in an oil bath for 6 h. After cooling to room temperature, the obtained membranes were rinsed with water several times and dried at 50 °C under vacuum. The CNF@Ni$(OH)_2$ hybrid membranes thus prepared with increasing $Ni(NO_3)_2·6H_2O$ concentrations were labeled as CNF@Ni$(OH)_2$-1, CNF@Ni$(OH)_2$-2, and CNF@Ni$(OH)_2$-3, respectively. For the preparation of CNF@NiS hybrid membranes, the CNF@Ni$(OH)_2$ hybrid membranes were transferred into a Teflon-lined autoclave containing 40 mL ethanol solution of thioacetamide (120 mg) and heated in an oven at 120 °C for 12 h. Correspondingly, the resulting CNF@NiS hybrid membranes were named as CNF@NiS-1, CNF@NiS-2, and CNF@NiS-3, respectively. For the control experiment, pure $Ni(OH)_2$ and NiS were also prepared via the same procedure without addition of CNF membranes.

Characterization: Morphology of the samples was investigated using FESEM (Ultra 55, Zeiss) at an acceleration voltage of 5 kV. XRD patterns of the samples were conducted on an X'Pert Pro X-ray diffractometer with Cu Kα radiation ($\lambda = 0.1542$ nm) under a voltage of 40 kV and a current of 40 mA. XPS analyses were carried out on an RBD upgraded PHI-5000C ESCA system (Perkin Elmer) with Mg Kα radiation ($h\nu = 1253.6$ eV) or Al Kα radiation ($h\nu = 1486.6$ eV). All XPS spectra were corrected using C1s line at 284.6 eV while curve fitting and background subtraction were accomplished using RBD AugerScan 3.21 software. TGA (Pyris 1) was performed under air flow from 100 to 800 °C at a heating rate of 10 °C min^{-1}. Raman spectra were measured on an Avalon Instruments Raman Station with a 532 nm laser as an excitation source. The BET surface area was measured using a Belsorp-max surface area detecting instrument by N_2 physisorption at 77 K.

Electrochemical Measurements: Electrochemical experiments were carried out with 2025 coin-type half-battery cells assembled in an argon-filled glovebox (M. Braun Inert gas Systems Co. Ltd.). Pure lithium foil was served as the counter and reference electrodes, while a polypropylene film (Celgard-2400) was used as the separator. The electrolyte was consisted of a solution of 1 M $LiPF_6$ in EC/DMC/DEC (1:1:1 by volume). The as-prepared self-standing CNF@NiS core/sheath hybrid membranes were directly used as anodes without adding any polymer binders or carbon black. In contrast, the pure NiS anodes were prepared by a slurry coating procedure. The slurry is consisted of NiS, acetylene black, and poly(vinylidene fluoride) dissolved in *N*-methyl-2-pyrrolidinone at a weight ratio of 8:1:1, respectively. The as-prepared slurry was pasted on pure copper foil and dried at 80 °C under vacuum. The cells were assembled in an argon-filled glovebox with the concentrations of moisture and oxygen below 0.1 ppm. CV curves were collected on a CHI660D electrochemical workstation (Chenhua Instruments Co. Ltd.) in the potential range from 0.01 to 3.0 V at a scan rate of 0.1 mV s^{-1}. The galvanostatic discharge–charge measurements and rate-performance tests under different current densities were performed in the voltage range from 0.01 to 3.0 V by using a CT2013A cell test instrument (LAND Electronic Co. Ltd.). The EIS was measured in the frequency range from 100 kHz to 0.01 Hz at open circuit potential with an AC voltage amplitude of 5.0 mV.

Supporting Information

Supporting Information is available from the Wiley Online Library or from the author.

Acknowledgements

The authors are grateful for financial support from the National Natural Science Foundation of China (Grant Nos. 51125011 and 51433001).

Received: August 24, 2015
Revised: September 30, 2015

[1] L. Wang, Y. J. Ye, X. P. Lu, Z. B. Wen, Z. Li, H. Q. Hou, Y. H. Song, *Sci. Rep.* **2013**, *3*, 3568.
[2] C. Z. Yuan, H. B. Wu, Y. Xie, X. W. Lou, *Angew. Chem., Int. Ed.* **2014**, *53*, 1488.
[3] L. L. Liu, Z. Q. Niu, L. Zhang, W. Y. Zhou, X. D. Chen, S. S. Xie, *Adv. Mater.* **2014**, *26*, 4855.
[4] L. F. Shen, L. Yu, X. Y. Yu, X. G. Zhang, X. W. Lou, *Angew. Chem., Int. Ed.* **2015**, *54*, 1868.
[5] Y. F. Zhao, W. Ran, J. He, Y. Z. Huang, Z. F. Liu, W. Liu, Y. F. Tang, L. Zhang, D. W. Gao, F. M. Gao, *Small* **2015**, *11*, 1310.
[6] T. Zhu, H. B. Wu, Y. B. Wang, R. Xu, X. W. Lou, *Adv. Energy Mater.* **2012**, *2*, 1497.
[7] P. G. Bruce, B. Scrosati, J. M. Tarascon, *Angew. Chem., Int. Ed.* **2008**, *47*, 2930.
[8] C. F. Zhang, Z. X. Chen, Z. P. Guo, X. W. Lou, *Energy Environ. Sci.* **2013**, *6*, 974.
[9] X. H. Cao, Y. M. Shi, W. H. Shi, X. H. Rui, Q. Y. Yan, J. Kong, H. Zhang, *Small* **2013**, *9*, 3433.
[10] J. H. Kong, W. A. Yee, Y. F. Wei, L. P. Yang, J. M. Ang, S. L. Phua, S. Y. Wong, R. Zhou, Y. L. Dong, X. Li, X. H. Lu, *Nanoscale* **2013**, *5*, 2967.
[11] J. Liang, X. Y. Yu, H. Zhou, H. B. Wu, S. J. Ding, X. W. Lou, *Angew. Chem., Int. Ed.* **2014**, *53*, 12803.
[12] Y. X. Tang, Y. Y. Zhang, J. Y. Deng, J. Q. Wei, H. L. Tam, B. K. Chandran, Z. L. Dong, Z. Chen, X. D. Chen, *Adv. Mater.* **2014**, *26*, 6111.
[13] W. H. Li, M. S. Li, Z. Z. Yang, J. Xu, X. W. Zhong, J. Q. Wang, L. C. Zeng, X. W. Liu, Y. Jiang, X. Wei, L. Gu, Y. Yu, *Small* **2015**, *11*, 2762.

[14] C. C. Xing, D. Zhang, K. Cao, S. M. Zhao, X. Wang, H. Y. Qin, J. B. Liu, Y. Z. Jiang, L. Meng, *J. Mater. Chem. A* **2015**, *3*, 8742.
[15] Z. M. Wan, J. Shao, J. J. Yun, H. Y. Zheng, T. Gao, M. Shen, Q. T. Qu, H. H. Zheng, *Small* **2014**, *10*, 4975.
[16] X. Xu, Z. Y. Fan, S. J. Ding, D. M. Yu, Y. P. Du, *Nanoscale* **2014**, *6*, 5245.
[17] G. Wang, J. Peng, L. L. Zhang, J. Zhang, B. Dai, M. Y. Zhu, L. L. Xia, F. Yu, *J. Mater. Chem. A* **2015**, *3*, 3659.
[18] X. Huang, Z. Y. Zeng, H. Zhang, *Chem. Soc. Rev.* **2013**, *42*, 1934.
[19] Y. M. Chen, Z. Li, X. W. Lou, *Angew. Chem., Int. Ed.* **2015**, *54*, 10521.
[20] L. F. Shen, L. Yu, H. B. Wu, X. Y. Yu, X. G. Zhang, X. W. Lou, *Nat. Commun.* **2015**, *6*, 6694.
[21] T. Zhu, Z. Y. Wang, S. J. Ding, J. S. Chen, X. W. Lou, *RSC Adv.* **2011**, *1*, 397.
[22] N. Mahmood, C. Z. Zhang, Y. L. Hou, *Small* **2013**, *9*, 1321.
[23] Z. J. Zhang, H. L. Zhao, Z. P. Zeng, C. H. Gao, J. Wang, Q. Xia, *Electrochim. Acta* **2015**, *155*, 85.
[24] X. Y. Yu, L. Yu, B. H. Wu, X. W. Lou, *Angew. Chem., Int. Ed.* **2015**, *54*, 5331.
[25] Y. Wang, Q. S. Zhu, L. Tao, X. W. Su, *J. Mater. Chem.* **2011**, *21*, 9248.
[26] L. W. Mi, Q. Ding, W. H. Chen, L. Zhao, H. W. Hou, C. T. Liu, C. Y. Shen, Z. Zheng, *Dalton Trans.* **2013**, *42*, 5724.
[27] S. T. Sebastian, R. S. Jagan, R. Rajagoplan, A. Paravannoor, L. V. Menon, K. Subramanian, S. V. Nair, A. Balakrishnan, *RSC Adv.* **2014**, *4*, 11673.
[28] J. H. Kong, C. Y. Zhao, Y. F. Wei, S. L. Phua, Y. L. Dong, X. H. Lu, *J. Mater. Chem. A* **2014**, *2*, 15191.
[29] Y. X. Tang, Y. Y. Zhang, J. Y. Deng, D. P. Qi, W. R. Leow, J. Q. Wei, S. Y. Yin, Z. L. Dong, R. Yazami, Z. Chen, X. D. Chen, *Angew. Chem., Int. Ed.* **2014**, *53*, 13488.
[30] G. X. Gao, H. B. Wu, S. J. Ding, X. W. Lou, *Small* **2015**, *11*, 432.
[31] L. B. Ma, X. P. Shen, Z. Y. Ji, S. Wang, H. Zhou, G. X. Zhu, *Electrochim. Acta* **2014**, *146*, 525.
[32] H. C. Tao, X. L. Yang, L. L. Zhang, S. B. Ni, *J. Electroanal. Chem.* **2015**, *739*, 36.
[33] M. Y. Son, J. H. Choi, Y. C. Kang, *J. Power Sources* **2014**, *251*, 480.
[34] K. Aso, A. Hayashi, M. Tatsumisago, *Electrochim. Acta* **2012**, *83*, 448.
[35] K. Aso, A. Sakuda, A. Hayashi, M. Tatsumisago, *ACS Appl. Mater. Interfaces* **2013**, *5*, 686.
[36] Z. Q. Wang, X. Li, Y. Yang, Y. J. Cui, H. G. Pan, Z. Y. Wang, B. L. Chen, G. D. Qian, *J. Mater. Chem. A* **2014**, *2*, 7912.
[37] Q. Pan, J. Xie, S. Y. Liu, G. S. Cao, T. J. Zhu, X. B. Zhao, *RSC Adv.* **2013**, *3*, 3899.
[38] H. Geng, S. F. Kong, Y. Wang, *J. Mater. Chem. A* **2014**, *2*, 15152.
[39] H. C. Ruan, Y. F. Li, H. Y. Qiu, M. D. Wei, *J. Alloys Compd.* **2014**, *588*, 357.
[40] Y. E. Miao, Y. P. Huang, L. S. Zhang, W. Fan, F. L. Lai, T. X. Liu, *Nanoscale* **2015**, *7*, 11093.
[41] Y. E. Miao, G. N. Zhu, H. Q. Hou, Y. Y. Xia, T. X. Liu, *J. Power Sources* **2013**, *226*, 82.
[42] Y. Si, X. M. Tang, J. L. Ge, S. Yang, M. El-Newehy, S. S. Al-Deyab, J. Y. Yu, B. Ding, *Nanoscale* **2014**, *6*, 2102.
[43] F. L. Lai, Y. E. Miao, Y. P. Huang, T. S. Chung, T. X. Liu, *J. Phys. Chem. C* **2015**, *119*, 13442.
[44] A. Abbasi, M. M. Nasef, M. Takeshi, R. Faridi-Majidi, *Chin. J. Polym. Sci.* **2014**, *32*, 793.
[45] L. Cao, D. F. Su, Z. Q. Su, X. N. Chen, *Chin. J. Polym. Sci.* **2014**, *32*, 1167.
[46] L. Yu, L. Zhang, H. B. Wu, X. W. Lou, *Angew. Chem., Int. Ed.* **2014**, *53*, 3711.
[47] L. W. Mi, Y. F. Chen, W. T. Wei, W. H. Chen, H. W. Hou, Z. Zheng, *RSC Adv.* **2013**, *3*, 17431.
[48] K. Aso, A. Hayashi, M. Tatsumisago, *New J. Chem.* **2014**, *38*, 1731.
[49] N. H. Idris, M. M. Rahman, S. L. Chou, J. Z. Wang, D. Wexler, H. K. Liu, *Electrochim. Acta* **2011**, *58*, 456.
[50] X. H. Xia, C. R. Zhu, J. S. Luo, Z. Y. Zeng, C. Guan, C. F. Ng, H. Zhang, H. J. Fan, *Small* **2014**, *10*, 766.
[51] G. F. Zou, D. W. Zhang, C. Dong, H. Li, K. Xiong, L. F. Fei, Y. T. Qian, *Carbon* **2006**, *44*, 828.
[52] C. G. Li, H. Yi, T. Jalalabadi, D. Lee, *J. Power Sources* **2015**, *294*, 284.
[53] H. W. Nesbitt, D. Legrand, G. M. Bancroft, *Phys. Chem. Miner.* **2000**, *27*, 357.
[54] F. Loglio, M. Innocenti, A. Jarek, S. Caporali, I. Pasquini, M. L. Foresti, *J. Electroanal. Chem.* **2010**, *638*, 15.
[55] S. B. Ni, X. L. Yang, T. Li, *J. Mater. Chem.* **2012**, *22*, 2395.